Available online at www.sciencedirect.com

ScienceDirect

journal homepage: www.elsevier.com/locate/he

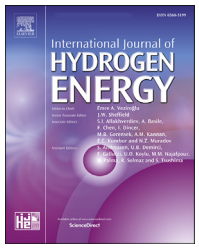

Microstructure and first hydrogenation properties of TiFe alloy with Zr and Mn as additives

Abhishek Kumar Patel [a,b], *Alexandre Duguay* [a], *Bernard Tougas* [c], *Chris Schade* [d], *Pratibha Sharma* [b], *Jacques Huot* [a,*]

[a] *Hydrogen Research Institute, Université Du Québec à Trois-Rivières, 3351 des Forges, Québec, G9A 5H7, Canada*
[b] *Department of Energy Science & Engineering, Indian Institute of Technology Bombay, Mumbai, Maharashtra, 400076, India*
[c] *Centre de Métallurgie Du Québec (CMQ), 3095, Rue Westinghouse, Trois-Rivières, Québec, G9A 5E1, Canada*
[d] *GKN Powder Metallurgy, Germany*

HIGHLIGHTS

- TiFe doped with only Zr or only Mn or combination of Zr + Mn was studied.
- Combination of 2 wt% Mn + 4 wt% Zr had the highest capacity ~2 wt%.
- Fast first hydrogenation is due to the presence of Ti_2Fe type phase.

ARTICLE INFO

Article history:
Received 12 July 2019
Received in revised form
22 October 2019
Accepted 27 October 2019
Available online 28 November 2019

Keywords:
TiFe alloy
Morphology
Activation kinetics
Hydrogen storage

ABSTRACT

In this paper, the effect of Zr and Mn on the microstructure and first hydrogenation kinetic of TiFe alloy is reported. TiFe alloy to which Zr, Mn or a combination of both have been added were synthesized by induction melting. First hydrogenation of all alloys was performed at room temperature under 20 bar of hydrogen. We found that addition of manganese makes possible activation at room temperature, but kinetics was very sluggish. Alloy with 2 wt% Zr did not absorb hydrogen. However, with addition of 4 wt% Zr, the alloy absorbed 1.2 wt% of hydrogen. A synergetic effect was found when zirconium was added along with manganese. Alloy with 1 wt% Mn and 2 wt% Zr had better kinetics than the alloy having only Mn or only Zr. The maximum hydrogen capacity was also greater at ~1.8 wt% after 7 h. Combination of 4 wt% Zr and 2 wt% Mn absorbed 2 wt% of hydrogen in 5 h. The rate limiting step for each activated alloy was found to be diffusion controlled with decreasing interface velocity.

Introduction

Emission of greenhouse gases due to the intensive use of fossils fuel demands the development of alternative fuels [1,2]. Hydrogen fulfills the criteria as an alternative energy carrier due to its high energy density, availability and less impact on the environment when produced by renewable resources such as solar and wind energies [3,4]. One of the major challenges in the development of hydrogen economy is

* *Corresponding author.*
E-mail addresses: abhishek.patel@iitb.ac.in (A.K. Patel), alexandre.duguay@uqtr.ca (A. Duguay), bernard.tougas@cegeptr.qc.ca (B. Tougas), pratibha_sharma@iitb.ac.in (P. Sharma), jacques.huot@uqtr.ca (J. Huot).
https://doi.org/10.1016/j.ijhydene.2019.10.239

to store hydrogen safely and at low cost [5]. The solid-state hydrogen storage in metal hydrides presents some advantages over the conventional high-pressure cylinders and liquid hydrogen because of its high volumetric capacity, low pressure, and low temperature of operation [6–10]. Metal hydrides can also be used as a negative electrode in rechargeable batteries such as Ni-MH [11–13]. Two of the major characteristics of metal hydrides should have in order to fulfill the requirements for mobile and stationary applications are low cost and utilization in a practical range of temperature and pressure (0–100 °C, 1–10 atm) [14–16]. TiFe alloy is a promising candidate to meet these requirements. TiFe alloy has low cost of raw material, good hydrogen capacity (maximum hydrogen capacity ~1.9 wt%) and works at room temperature under mild pressure [17]. For example, TiFe-based alloy is presently used in the fuel cell powered submarines [18]. However, one difficulty with TiFe alloy for hydrogen storage is the very slow first hydrogenation due to the presence of surface oxide layer which acts as a barrier for hydrogen gas [19,20]. In earlier literature, mechanical alloying [21–26] and severe plastic deformation techniques [27,28] have been used on TiFe alloy for the enhancement of activation process. Change in chemical composition by adding other elements such as Cu [29], Ce [30], Pd [31], Al, Ni, Co [32], Mn [33,34], Zr [35–37] also eases the first hydrogenation and improves kinetics. Recently, Peng et al. found that addition of 4 wt% (Zr + 2 Mn) to TiFe alloy improves the activation of TiFe alloy but kinetics is still slow [38]. This justified the study of the effect of individual elements (Zr, Mn) as dopant and also combination of these two elements on the kinetics of first hydrogenation of TiFe alloy. These two elements were selected because Zr is very effective to enhance the first hydrogenation and Mn is a well-known catalyst for hydrogenation of various metal hydrides. A combination of these elements has been made in order to study a possible synergy between Zr and Mn.

Experimental details

Ingots of TiFe with and without additive were synthesized by GKN Powder Metallurgy. The synthesis was done by induction melting under vacuum using industrial grade Fe (ASTM 1005) and Ti (ASTM B265 grade 1). The melt size was ~6.5 kg. The additives were Zr 702 (99.2%) alloy and electrolytic manganese Mn (99.7%). The bulk composition of all alloys, as measured by X-ray fluorescence spectrometer (Bruker XRF S1titan), is shown in Table 1 and compared with the nominal composition of each alloy. The measured composition is close to the nominal one but, it is seen that for manganese containing alloys the amount of titanium is higher and iron lower than the nominal values. In fact, this discrepancy seems to get bigger as manganese concentration increases.

It must be mentioned here that this work differs from the previous investigation [33,34]. Previously, partial substitution of Mn for Fe in TiFe had been investigated while in the present paper, elements are added to stoichiometric TiFe. Furthermore, in these previous investigations, the alloy was heat treated prior to activation. In the study presented here, no heat treatment was applied to the alloy.

In the present work, TiFe with addition of 1 wt% or 6 wt% Mn has been synthesized at large scale (~6.5 kg). First hydrogenation was carried out without any prior heat treatment. A comparison with the previous studies on the addition of Zr and addition of a combination of Zr and Mn to TiFe alloy is summarized in Table 2. There are strong similarities between the alloys reported in Table 2 and other investigations of TiFe alloys and the alloys reported in this paper. However, the following discrepancies should be pointed out. First, the starting Ti and Fe elements were of industrial grades. Usually, laboratory grades are used but here we wanted to test alloys that were synthesized at large scale. In this work, casting of alloys was done at large scale (~6.5 kg) contrary to the vast majority of other investigations where casting is of laboratory scale (~3 g). Again, this was to be as close as possible to realistic industrial conditions. Also, in the present investigation, Zr and Mn are added to TiFe alloy while in most investigations they are substituted to either Ti or Fe or both.

The synthesized ingots of each alloy were crushed in air to obtain small chunks. These small chunks were thereafter crushed into powder in an argon atmosphere using a hardened steel mortar and pestle. First hydrogenation tests were performed at room temperature and under a hydrogen pressure of 20 bar in a homemade Sievert apparatus. 1 g of sample was filled in the reactor in argon atmosphere and reactor

Table 1 – Bulk chemical analysis: nominal and as measured by XRF (X-ray fluorescence) spectrometer of all alloys. Uncertainty on all values is ±1 at. %.

Alloy		Ti (at. %)	Fe (at. %)	Zr (at. %)	Mn (at. %)
TiFe	Nominal composition	50	50		
	Measurement	50	50		
TiFe +2 wt% Zr	Nominal composition	50	49	1	
	Measurement	50	48	1	
TiFe +4 wt% Zr	Nominal composition	49	49	2	
	Measurement	50	48	2	
TiFe +1 wt% Mn	Nominal composition	50	49		<1
	Measurement	51	47		1
TiFe +6 wt% Mn	Nominal composition	47	47		6
	Measurement	52	42		6
TiFe +1 wt% Mn + 2 wt% Zr	Nominal composition	49	49	1	<1
	Measurement	55	43	1	<1
TiFe +2 wt% Mn + 4 wt% Zr	Nominal composition	48	48	2	2
	Measurement	53	42	2	2

Table 2 – The difference between the current work and previous investigations.

Literature	Starting materials	Hydrogen capacity (wt.%)	Heat Treatment	Melt size
Jain et al. [35] TiFe + 4 wt% Zr	Ti (99.9%, sponge), Fe (99.5%, pieces), Zr (99.5%, sponge)	1.6 (20 bar, 40 °C)	no	Laboratory scale (~3 g)
Peng et al. [36] $TiFeZr_{0.05}$	purchased from Alfa Aesar	1.4 (20 bar, room temperature)		
Patel et al. [37] TiFe + 4 wt% Zr	Industrial grade Ti (ASTM B265 grade 1), Fe (ASTM 1005), Zr (99.5%, sponge)	1.6 wt% (20 bar, room temperature)		
This work TiFe + x wt% Zr (x = 2, 4)	Industrial grade Ti (ASTM B265 grade 1), Fe (ASTM 1005), Zr 702 (99.2%)	For 2 wt% Zr No activation (20 bar, room temperature) For 4 wt% Zr 1.2 (20 bar, room temperature)		Large scale (~6.5 kg)
Peng et al. [38] Addition of 4 wt% (Zr + 2 Mn) to TiFe	Ti (99.9%, sponge), Fe (99.5%, pieces), Zr (99.5%, sponge) purchased from Alfa Aesar	0.9 (30 bar, room temperature)		Laboratory scale (~3 g)
This work TiFe + 2 wt% Mn + 4 wt% Zr	Industrial grade Ti (ASTM B265 grade 1), Fe (ASTM 1005), Zr 702 (99.2%)	2 (20 bar, room temperature)		Large scale (~6.5 kg)

temperature was controlled using an air furnace. To have a better heat conductivity and also a bigger thermal mass, an annulus of copper was in close thermal contact to the reactor. This restricted the temperature change during hydrogenation or dehydrogenation to a few degrees at maximum. A Hitachi SU-3500 scanning electron microscope (SEM) equipped with an EDX (Energy Dispersive X-ray) spectrometer from Oxford Instruments was utilized to investigate the microstructure and chemical composition of each alloy. Samples for SEM observations were prepared by polishing small chunks of alloys embedded into epoxy resin. X-ray pattern of each alloy was obtained using a Bruker D8 Focus X-ray with Cu kα radiation. The scanning speed for X-ray diffraction pattern measurements was 0.04°/sec. Rietveld refinement was performed on the X-ray patterns using Topas software [39]. The phase identification and Rietveld analysis for TiFe, Ti and $TiFe_2$ phase was done by using the reference phases present in phase diagram of Ti–Fe system [40]. For Ti_2Fe, reference [41] was used.

Result and discussion

Morphology

Fig. 1 shows the microstructure of all the compositions studied. We could clearly see small secondary phase, bright grey phase over a uniform grey phase, in the pure TiFe alloy. It should be pointed out that, for pure TiFe alloy, the secondary phase abundance was very small. Fig. 1(a) is a close-up of a region with secondary phase but is not representative of the whole alloy. The other compositions had a more uniform distribution of the secondary phases. The TiFe alloys with only Zr additive (2 wt% and 4 wt%) have grey phase, light grey phase, and a bright phase. The alloy with 2 wt% Zr has much more globular secondary phase compared to the 4 wt% Zr alloy. In the case of 2 wt% Zr, the bright phase is found to be at the edge of light grey phase. However, in the microstructure of TiFe alloy with 4 wt% Zr, the bright phase is more clearly embedded in the light grey phase. The microstructure of alloys with only Mn as additive is shown in Fig. 1(d), (e). For low doping level (1 wt% Mn), we see black precipitates and islands of dark grey phase within the main grey phase. For 6 wt% Mn alloy, the black precipitates are very small. Fig. 1(f), (g) show the microstructure of alloy doped with Zr and Mn simultaneously.

For the addition of 1 wt% Mn and 2 wt% Zr (Fig. 1f), the alloy is made of a main grey phase and a secondary phase that is brighter at its edge. This change of brightness within the secondary phase indicates a variation in chemical composition. A similar situation is seen in alloy with 2 wt% Mn and 4 wt% Zr (Fig. 1g) but with a much more abundant secondary phase. Also, closer inspection (Fig. 2) shows stripes of dark phase inside the secondary phase.

The chemical composition of each phase was evaluated by EDX analysis. In Fig. 3, elemental mapping using EDX is shown for TiFe alloy. Area analysis of the grey and bright grey phases are presented in Table 3. It shows that the bright grey phase has a chemical composition very close to $TiFe_2$ which is a phase expected from the phase diagram.

Fig. 4 shows the area analysis of each phase present in alloys doped with 2 and 4 wt% Zr. The chemical composition of each phase is shown in Table 4. This confirms that the main grey phase is TiFe. For both alloys, zirconium is essentially concentrated in the bright phase. Bright phase has an average composition close to Ti 40 at. %, Fe 40 at. % and Zr 20 at.%. The light grey phase has a different chemical composition in the two alloys.

For 2 wt% Zr, light grey phase's composition is close to $TiFe_2$ while for 4 wt% Zr, it is close to Ti_2Fe. However, it is clear

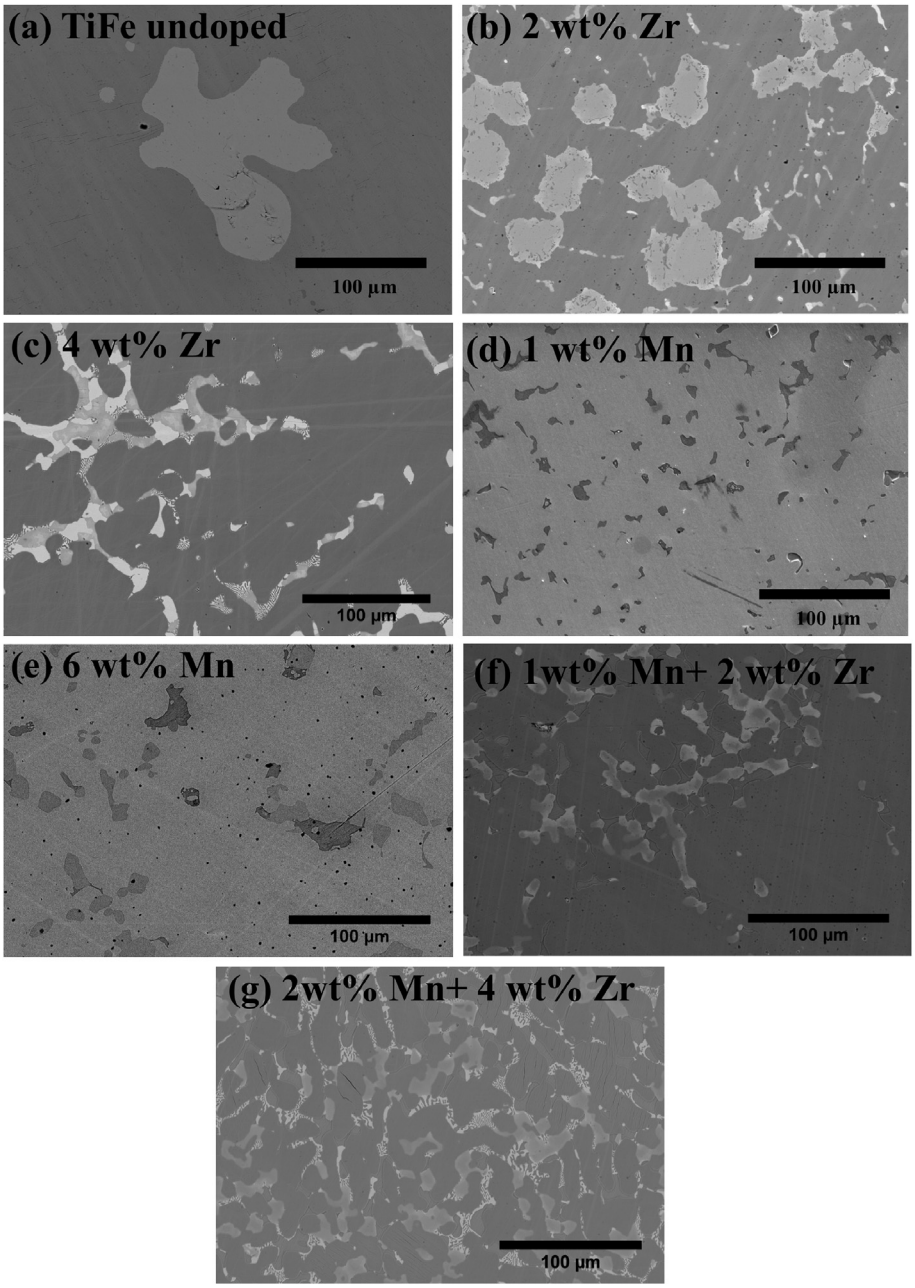

Fig. 1 – Microstructure of (a) as-cast TiFe alloy, TiFe with (b) 2 wt% Zr, (c) 4 wt% Zr, (d) 1 wt% Mn, (e) 6 wt % Mn, (f) 1 wt% Mn + 2 wt% Zr and (g) 2 wt% Mn + 4 wt% Zr.

from the micrographs that the bright phase and light grey phase are closely related. One explanation is that during solidification, zirconium is 'expelled' from the light grey phase to form the bright phase.

Fig. 5 shows the EDX analysis of TiFe alloys doped with Mn at a concentration level of 1 and 6 wt%.

Table 5 shows the chemical composition of TiFe alloys doped with Mn. As in the preceding cases, the grey phase is TiFe but here, as Mn content increases, the concentration of Mn in TiFe phase increases. It is also clear that manganese substitute for iron. Light grey phase has a composition close to Ti_2Fe. Dark grey phase is a Ti-rich phase.

Fig. 6 shows the EDX analysis of alloy having Zr and Mn. The first alloy has 1 wt% Mn and 2 wt% Zr. The second alloy has twice this concentration. There are three phases present in each alloy: (1) grey phase; (2) light grey phase and (3) bright phase. The chemical composition of each phase is shown in Table 6. As for the other alloys, the grey phase is TiFe. Since, as manganese is one of the additives, the TiFe phase has some manganese that is substituted for iron.

Light grey and bright phases are Zr-rich phases. The bright phase has a higher proportion of Zr compare to the other two phases. We also see that the light grey phase has Zr abundance about ½ of the abundance in the bright phase.

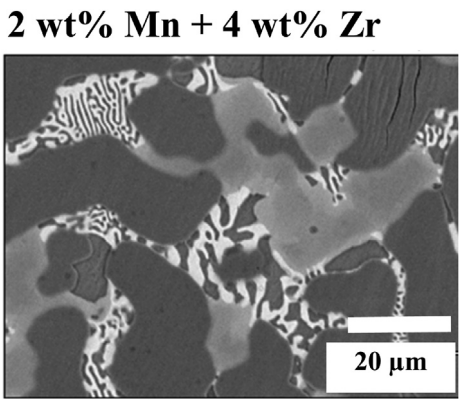

Fig. 2 – Microstructure of TiFe +2 wt% Mn + 4 wt% at 20 µm scale.

Structural characterization

Fig. 7 shows the X-ray pattern of each alloy and confirms the presence of a main TiFe (space group Pm-3m) phase with, in most alloys, secondary phases of $TiFe_2$ type (space group $P6_3/mmc$), Ti_2Fe type (space group Fd-3m) and Ti (space group $P6_3/mmc$). In the Rietveld refinement, the crystallite size and lattice parameter have been evaluated and the results are shown in Table 7. Phase fraction was also measured by Rietveld refinement for each phase in each alloy (Table 7).

X-ray pattern of TiFe undoped reveals a main TiFe phase with some minor peaks attributed to $TiFe_2$. The presence of these phases in TiFe undoped is also evidenced by the result of chemical composition analysis of TiFe alloy as shown in Table 3.

Table 3 – Chemical composition of different phases present in TiFe (uncertainty on all values is ±1).

TiFe	Ti (at. %)	Fe (at. %)
Area 1 (grey phase)	50	50
Area 2 (bright grey phase)	40	60

For the alloy doped with 2 wt% Zr, presence of TiFe and $TiFe_2$ phases could be seen. At concentration level of 4 wt% Zr, appearance of minors peaks related to Ti_2Fe phase could be seen along with TiFe main phase. Presence of these phases is in good agreement with the chemical composition analysis of alloys with only Zr (Table 4). The main cause of the appearance of Ti_2Fe phase was that addition of Zr at concentration level of 4 wt% leads to the formation of Ti-rich phase. X-ray pattern of TiFe alloy with only Mn (6 wt%) shows a major peak of TiFe alloy with minor peak of Ti_2Fe. However, at 1 wt% level of Mn, minor peak of Ti_2Fe totally disappeared. The main cause of presence of Ti_2Fe phase along with TiFe in the alloy with 6 wt% Mn only is that addition of Mn leads to a significant reduction of $TiFe_2$ phase and the formation of Ti-rich phase as recently found by Shang et al. [42].

Minor peaks of Ti and Ti_2Fe phases were observed in the X-ray pattern of TiFe alloy with the combination of Zr and Mn. These minor phases were also seen in chemical composition analysis of alloys with the combination of Zr and Mn. For the Ti_2Fe-like phase, a close inspection of the EDX results of Table 6 shows that adding the abundance of Ti and Zr gives a total abundance very close to 66 at% while the abundance of Fe is close to 33 at.%. Thus, it indicates that, in this phase, zirconium seems to substitute for titanium. Lattice parameter is almost the same for each phase in all alloys. From Table 7, we

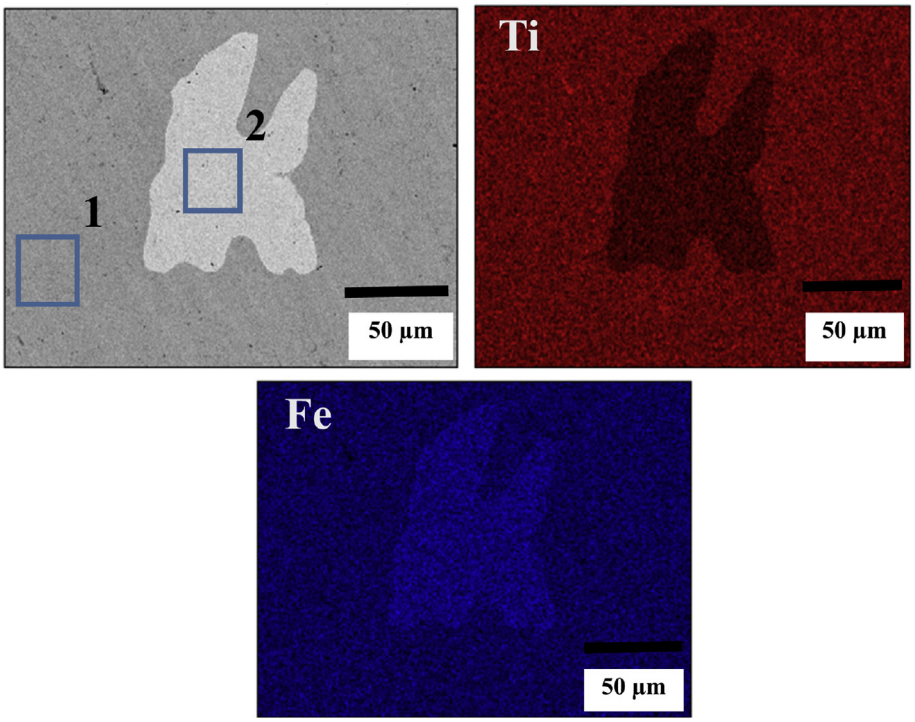

Fig. 3 – EDX analysis and elemental mapping of TiFe.

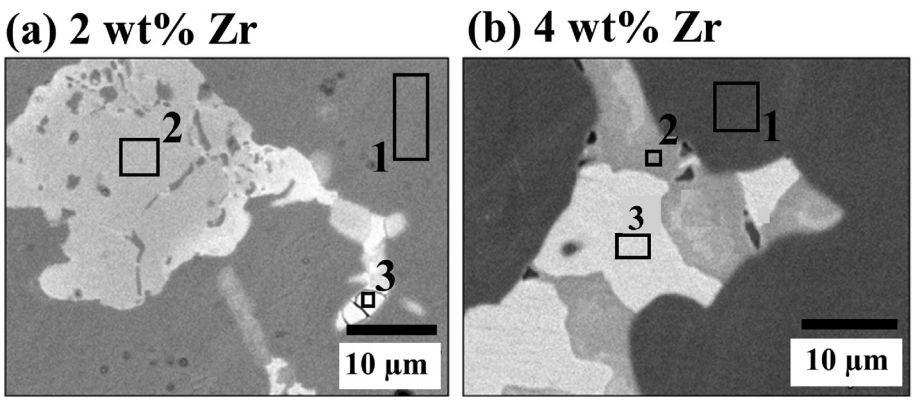

Fig. 4 – EDX analysis of TiFe doped with Zr (a) 2 wt% Zr and (b) 4 wt% Zr.

Table 4 – Chemical composition of each phase present in alloys doped with Zr (uncertainty on all values is ±1).

Alloys	Ti (at. %)	Fe (at. %)	Zr (at. %)
TiFe +2 wt% Zr			
Area 1 (grey phase)	50	50	
Area 2 (light grey phase)	39	58	3
Area 3 (bright phase)	39	42	17
TiFe + 4 wt% Zr			
Area 1 (grey phase)	51	49	<1
Area 2 (light grey phase)	56	33	12
Area 3 (bright phase)	43	37	20

Table 5 – Chemical composition of different phases present in each alloy having Mn (uncertainty on all values is ±1).

Alloy	Ti (at. %)	Fe (at. %)	Mn (at. %)
TiFe +1 wt% Mn			
Area 1 (grey phase)	52	48	<1
Area 2 (light grey phase)	67	33	<1
Area 3 (dark grey phase)	82	18	<1
TiFe + 6 wt% Mn			
Area 1 (grey phase)	51	43	6
Area 2 (light grey phase)	63	32	6
Area 3 (dark grey phase)	77	17	6

could see that the crystallite size of TiFe increases with the zirconium content. Unfortunately, because of the limited numbers of data points, the functional form of this increase could not be established. In the same way, addition of manganese increases the crystallite size of TiFe. In this case, the increase is higher than in the zirconium case. An opposite trend is seen for the $TiFe_2$ phase when only Zr is added to TiFe. We see that the crystallite size of this phase is smaller for 2 wt % Zr addition than for the TiFe alloy. The Ti_2Fe phase has a constant crystallite size for all alloys with Mn doping while the crystallite size is much smaller in the alloy with only Zr addition. It could be concluded that addition of Zr and Mn has an impact on the crystallite size of the phases present in the alloys.

Activation kinetics

First hydrogenation (activation) curves of TiFe alloy doped with Zr (2, 4 wt%), Mn (1, 6 wt%), with 2 wt% Mn + 4 wt% Zr and with 1 wt% Mn + 2 wt% Zr are shown in Fig. 8. As we could clearly see, TiFe without any dopant does not absorb hydrogen. Alloy having 2 wt% Zr could also not be activated.

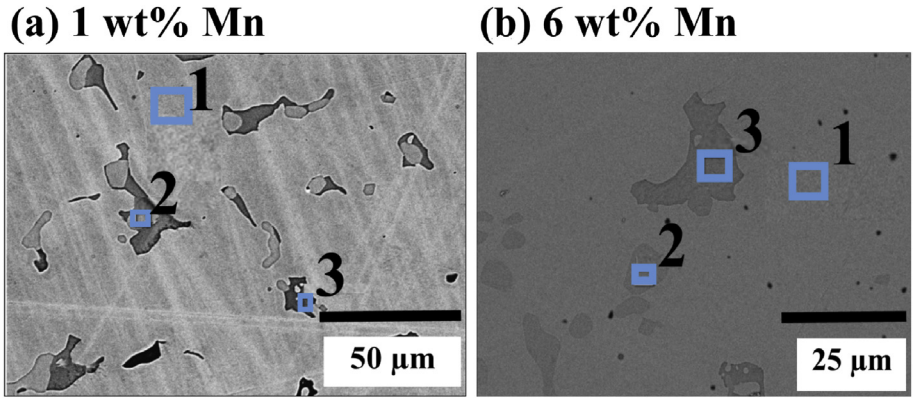

Fig. 5 – EDX analysis of TiFe alloy with Mn (a) 1 wt%, (b) 6 wt%.

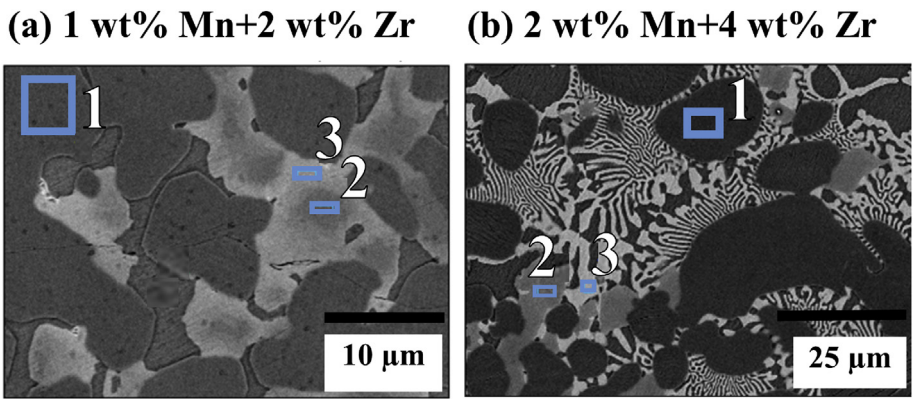

Fig. 6 – EDX analysis of TiFe alloy with Zr and Mn.

Table 6 – Chemical composition of different phases present in each alloy having Zr and Mn (uncertainty on all values is ±1).

Alloy	Ti (at. %)	Fe (at. %)	Zr (at. %)	Mn (at. %)
TiFe +1 wt % Mn + 2 wt % Zr				
Area 1(grey phase)	51	47		<1
Area 2 (light grey phase)	62	32	4	<1
Area 3 (bright phase)	56	32	11	<1
TiFe + 2 wt % Mn + 4 wt % Zr				
Area 1(grey phase)	50	47		3
Area 2 (light grey phase)	56	31	10	2
Area 3 (bright phase)	43	32	21	2

Addition of Zr only is beneficial but a minimum amount of Zr (~4 wt% Zr) is essential to activate under the present conditions.

The alloys with only Mn addition present an incubation time that increases with increasing Mn content. However, the maximum capacity increases with Mn content. Adding both Zr and Mn brings the benefits of both elements (i.e. no incubation time and better capacity). Clearly, there is some synergetic effect because the kinetics and capacities are much better than what could be achieved by just the sum of what was seen for Zr and Mn alone. The alloy with 2 wt% Mn and 4 wt% Zr has the fastest kinetics and highest capacity. Therefore, we could conclude that addition of Zr and Mn is beneficial for activation and hydrogen capacity of TiFe alloy.

The reason for the faster kinetics and higher capacity of the TiFe alloy with 2 wt% Mn + 4 wt % Zr could be related to the microstructure and chemical composition of the phases. From Fig. 1, we see that, compared to the other alloys, the secondary phase finely and homogeneously distributed within the TiFe alloy in the alloy with 2 wt% Mn + 4 wt% Zr. The chemical

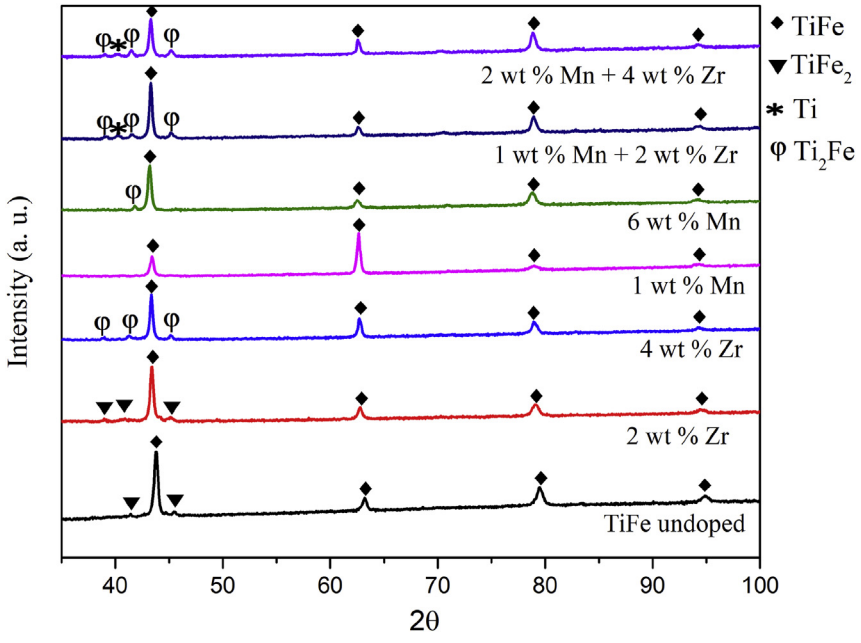

Fig. 7 – X-ray pattern of TiFe undoped and doped with Zr, Mn, and Zr + Mn alloys.

Table 7 – Phase fraction, lattice parameter and crystallite size for each alloy composition.

Phase name	Phase fraction (%)	Lattice parameter (Å)	Crystallite size (nm)
TiFe undoped			
TiFe	93(1)	a = 2.98(1)	31(1)
$TiFe_2$	7(1)	a = 4.71(1) c = 7.97(1)	36(2)
2 wt% Zr			
TiFe	89(1)	a = 2.98(1)	34(2)
$TiFe_2$	11(1)	a = 4.84(1) c = 8.10(1)	23(2)
4 wt% Zr			
TiFe	73(1)	a = 2.98(1)	41(2)
Ti_2Fe	27(1)	a = 11.48(1)	17(2)
1 wt% Mn			
TiFe	100(1)	a = 2.99(1)	40(1)
6 wt% Mn			
TiFe	90(1)	a = 2.99(1)	52(2)
Ti_2Fe	10(1)	a = 11.32(1)	45(1)
1 wt% Mn + 2 wt% Zr			
TiFe	79(1)	a = 2.99(1)	44(1)
Ti_2Fe	18(1)	a = 11.42(1)	45(2)
Ti	3(1)	a = 2.99(1) c = 4.67(1)	25(1)
2 wt% Mn + 4 wt% Zr			
TiFe	70(1)	a = 2.99(1)	33(1)
Ti_2Fe	28(1)	a = 11.44(1)	45(1)
Ti	2(1)	a = 2.99(1) c = 4.77(1)	20(2)

composition of the secondary phases also plays a role. For both TiFe +1 wt% Mn + 2 wt % Zr and TiFe +2 wt% Mn + 4 wt % Zr alloys, the diffraction patterns showed the presence of Ti and Ti_2Fe phases. It may be the presence of these phases that makes the first hydrogenation very quick and high capacity. Titanium could act as a gateway for hydrogen to enter the TiFe phase. However, more extensive study is needed to test this hypothesis. Guéguen et al. already showed the importance of Ti-rich (Ti_2Fe, Ti) phases for easy activation and improving kinetic [43].

Rate limiting step of first hydrogenation

A clear difference among the first hydrogenation kinetics of activated alloys could be seen in Fig. 9. Change in the rate limiting step may be the cause for the different first hydrogenation kinetics. The usual rate limiting step model equations are described in Table 8 which summarizes the chemisorption, nucleation-growth-impingement, contracting volume and Ginstling-Brounshtein models. The best way to know the rate limiting step is to do the linear regression for the plot of the left side of the equation as a function of time for each model. The best linear fitted model will give information about mechanism of hydrogenation. In these equations, X is the transformed factor which represents the ratio of the absorbed hydrogen quantity divided by the alloy's maximum hydrogen absorption capacity ($X = \%H/\%H_{max}$), k is the reaction constant and t is time. The linear regressions were performed for 10% to 90% of the transformed factor (X = 0.1 to 0.9) as shown in the previous rate limiting studies [44] and fitted curves are shown in Fig. 9 for each activated alloys. The adjusted R^2 values for the linear regression of each alloy's model curve are shown in Table 9. It shows that adjusted R^2 value for GB3D model is closer to 1 than any other model. It clearly shows a good linear fitting for the GB3D model. Therefore, rate limiting step for each activated alloy was found to be three-dimensional growth where diffusion controlled with decreasing interface velocity.

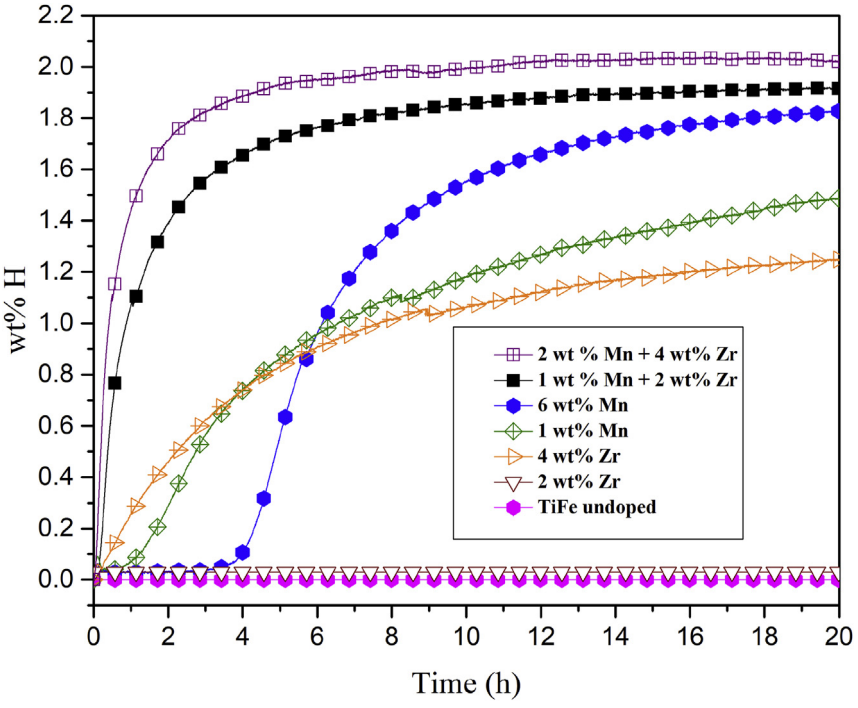

Fig. 8 – Activation kinetics of all alloys at room temperature under 20 bar hydrogen pressure.

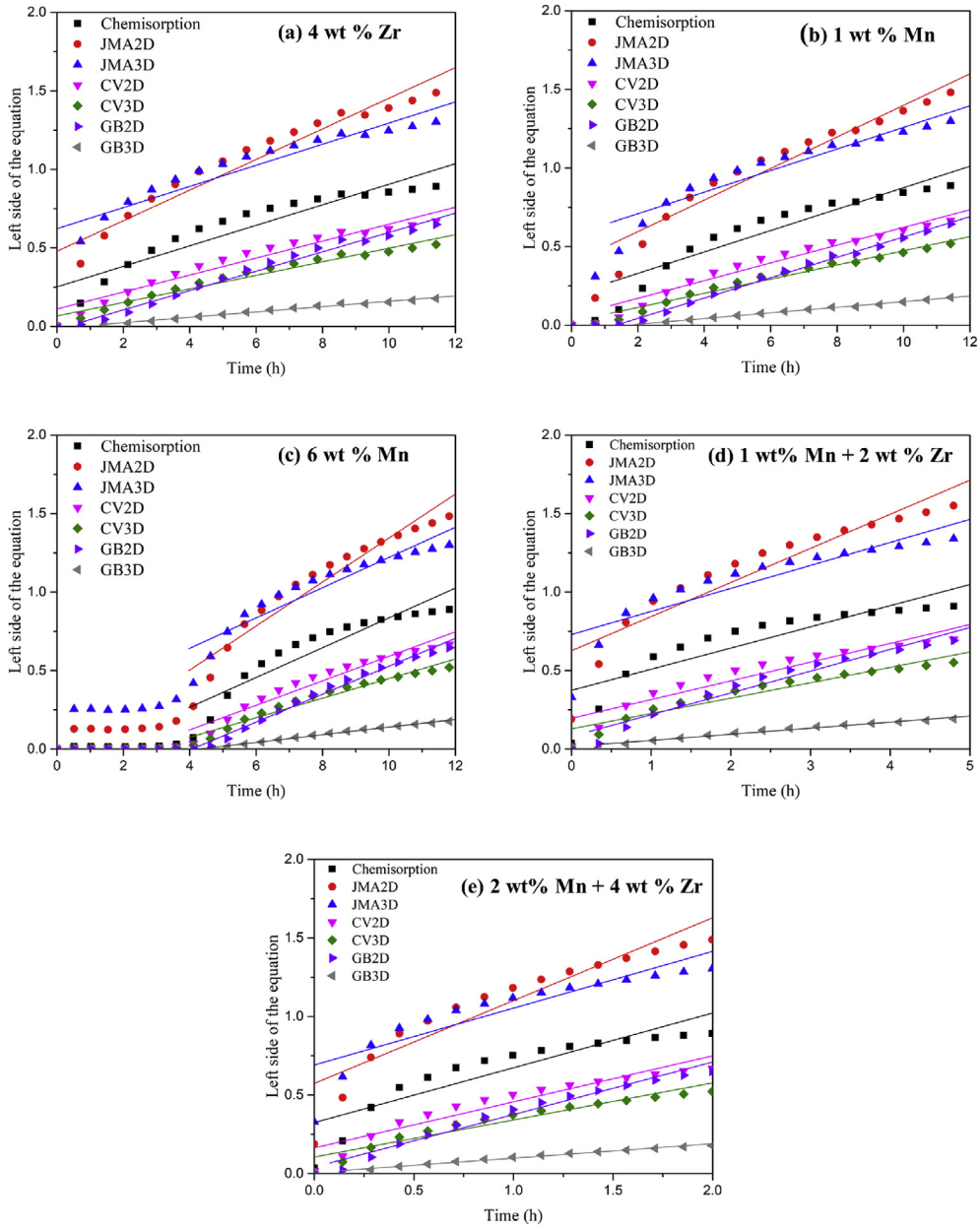

Fig. 9 – Linear fitting of each rate limiting step model for each activated alloy (a) for 4 wt % Zr, (b) 1 wt% Mn, (c) 6 wt% Mn, (d) 1 wt% Mn + 2 wt% Zr and (e) 2 wt% Mn + 4 wt% Zr.

Table 8 – Model equations for rate limiting step determination.

Rate limiting step model name	Model equation	Description
Chemisorption	$X = kt$	Surface controlled [45]
Nucleation-growth-impingement model (JMA2D)	$[-\ln(1-X)]^{1/2} = kt$	2D growth of existing nuclei with constant velocity [45,46]
Nucleation-growth-impingement model (JMA3D)	$[-\ln(1-X)]^{1/3} = kt$	3D growth of existing nuclei with constant velocity [45,46]
Contracting volume (CV2D)	$1-(1-X)^{1/2} = kt$	2D growth with constant interface velocity [45]
Contracting volume (CV3D)	$1-(1-X)^{1/3} = kt$	3D growth with constant interface velocity [45]
Ginstling-Brounshtein model (GB2D)	$(1-X)\ln(1-X) + X = kt$	2D growth, diffusion controlled with decreasing interface velocity [47]
Ginstling-Brounshtein model (GB3D)	$1-(2X/3) - (1-X)^{2/3} = kt$	3D growth, diffusion controlled with decreasing interface velocity [45]

Table 9 – Adjusted R^2 value for the linear regression of Model equations shown in Table 8.

Adjusted R^2	Chemisorption	JMA2D	JMA3D	CV2D	CV3D	GB2D	GB3D
4 wt% Zr	0.87440	0.93112	0.88798	0.944877	0.96724	0.98505	0.99031
1 wt% Mn	0.88476	0.94378	0.90872	0.95753	0.97452	0.98501	0.99745
6 wt% Mn	0.86447	0.92667	0.88734	0.94198	0.96201	0.98742	0.99415
1 wt % Mn + 2 wt% Zr	0.76697	0.86706	0.80557	0.89401	0.92768	0.96104	0.97969
2 wt % Mn + 4 wt% Zr	0.80465	0.87823	0.82225	0.90428	0.93182	0.97406	0.98631

Conclusion

Microstructure and activation kinetics of pure TiFe and with addition of Zr or Mn or a combination of Zr and Mn were studied. The following conclusion could be drawn:

1. Doping with zirconium is effective but a certain level of zirconium (4 wt%) is necessary.
2. Doping with 1 wt% Mn is effective, but kinetics is very sluggish.
3. Simultaneous addition of 1 wt% Mn + 2 wt% Zr to TiFe alloy results in better kinetics and hydrogen capacity compared to only Zr or Mn doped alloys. It absorbs 1.8 wt% of hydrogen in 7 h.
4. The fastest and highest capacity measured was for the TiFe alloy with simultaneous addition of 2 wt% Mn and 4 wt% Zr. Hydrogen capacity for this alloy was 2 wt%. This fast first hydrogenation kinetics is attributed to the presence of a large proportion of Ti_2Fe type phase into which zirconium substitute for titanium.
5. The rate limiting step during the first hydrogenation for activated alloys was found to be a three-dimensional growth where diffusion controlled with decreasing interface velocity.

This investigation was targeted mainly to the first hydrogenation. Future work will be on the thermodynamic and cycling properties of these alloys.

Acknowledgment

Abhishek K. Patel acknowledges for a fellowship from Queen Elizabeth Scholars (QES). We would also like to thank Quebec Metallurgy Center (CMQ) for SEM analysis.

Appendix A. Supplementary data

Supplementary data to this article can be found online at https://doi.org/10.1016/j.ijhydene.2019.10.239.

REFERENCES

[1] Höök M, Tang X. Depletion of fossil fuels and anthropogenic climate change: a review. Energy Policy 2013;52:797–809.
[2] Beer T, Grant T, Williams D, Watson H. Fuel-cycle greenhouse gas emissions from alternative fuels in Australian heavy vehicles. Atmos Environ 2002;36:753–63.
[3] Chaubey R, Sahu S, James OO, Maity S. A review on development of industrial processes and emerging techniques for production of hydrogen from renewable and sustainable sources. Renew Sustain Energy Rev 2013;23:443–62.
[4] Hosseini SE, Wahid MA. Hydrogen production from renewable and sustainable energy resources: promising green energy carrier for clean development. Renew Sustain Energy Rev 2016;57:850–66.
[5] Pudukudy M, Yaakob Z, Mohammad M, Narayanan B, Sopian K. Renewable hydrogen economy in Asia – opportunities and challenges: an overview. R Renew Sust Energy Rev 2014;30:743–57.
[6] Züttel A. Materials for hydrogen storage. Mater Today 2003;6:24–33.
[7] Sakintuna B, Lamari-Darkrim F, Hirscher M. Metal hydride materials for solid hydrogen storage: a review. Int J Hydrogen Energy 2007;32:1121–40.
[8] Callini E, Aguey-Zinsou K-F, Ahuja R, Ares JR, Bals S, Biliškov N, et al. Nanostructured materials for solid-state hydrogen storage: a review of the achievement of COST Action MP1103. Int J Hydrogen Energy 2016;41:14404–28.
[9] Rusman NAA, Dahari M. A review on the current progress of metal hydrides material for solid-state hydrogen storage applications. Int J Hydrogen Energy 2016;41:12108–26.
[10] Schneemann A, White JL, Kang S, Jeong S, Wan LF, Cho ES, et al. Nanostructured metal hydrides for hydrogen storage. Chem Rev 2018;118:10775–839.
[11] Zhao X, Ma L. Recent progress in hydrogen storage alloys for nickel/metal hydride secondary batteries. Int J Hydrogen Energy 2009;34:4788–96.
[12] Anik M. Electrochemical hydrogen storage capacities of Mg2Ni and MgNi alloys synthesized by mechanical alloying. J Alloy Comp 2010;491:565–70.
[13] Hapçı Ağaoğlu G, Orhan G. Production and electrochemical characterization of MgNi alloys by molten salt electrolysis for Ni–MH batteries. Int J Hydrogen Energy 2018;43:6266–74.
[14] Hoffman KC, Reilly JJ, Salzano FJ, Waide CH, Wiswall RH, Winsche WE. Metal hydride storage for mobile and stationary applications. Int J Hydrogen Energy 1976;1:133–51.
[15] Bellosta von Colbe J, Ares J-R, Barale J, Baricco M, Buckley C, Capurso G, et al. Application of hydrides in hydrogen storage and compression: achievements, outlook and perspectives. Int J Hydrogen Energy 2019;44:7780–808.
[16] Gambini M, Stilo T, Vellini M. Hydrogen storage systems for fuel cells: comparison between high and low-temperature metal hydrides. Int J Hydrogen Energy 2019;44:15118–34.
[17] Reilly JJ, Wiswall RH. Formation and properties of iron titanium hydride. Inorg Chem 1974;13:218–22.
[18] Psoma A, Sattler G. Fuel cell systems for submarines: from the first idea to serial production. J Power Sources 2002;106:381–3.
[19] Schlapbach L, Riesterer T. The activation of FeTi for hydrogen absorption. Appl Phys A 1983;32:169–82.
[20] Kim HC, Lee J-Y. A study on the activation mechanism of FeTi in view of surface conditions of metals. Int J Hydrogen Energy 1985;10:543–5.

[21] Falcão RB, Dammann EDCC, Rocha CJ, Durazzo M, Ichikawa RU, Martinez LG, et al. An alternative route to produce easily activated nanocrystalline TiFe powder. Int J Hydrogen Energy 2018;43:16107–16.
[22] Hosni B, Fenineche N, ElKedim O, Khaldi C, Lamloumi J. Structural and electrochemical properties of TiFe alloys synthesized by ball milling for hydrogen storage. J Solid State Electrochem 2018;22:17–29.
[23] Aoyagi H, Aoki K, Masumoto T. Effect of ball milling on hydrogen absorption properties of FeTi, Mg2Ni and LaNi5. J Alloy Comp 1995;231:804–9.
[24] Emami H, Edalati K, Matsuda J, Akiba E, Horita Z. Hydrogen storage performance of TiFe after processing by ball milling. Acta Mater 2015;88:190–5.
[25] Haraki T, Oishi K, Uchida H, Miyamoto Y, Abe M, Kokaji T, et al. Properties of hydrogen absorption by nano-structured FeTi alloys. Int J Mater Res 2008;99:507–12.
[26] Bellosta von Colbe JM, Puszkiel J, Capurso G, Franz A, Benz HU, Zoz H, et al. Scale-up of milling in a 100 L device for processing of TiFeMn alloy for hydrogen storage applications: procedure and characterization. Int J Hydrogen Energy 2019;44:29282–90.
[27] Edalati K, Matsuo M, Emami H, Itano S, Alhamidi A, Staykov A, et al. Impact of severe plastic deformation on microstructure and hydrogen storage of titanium-iron-manganese intermetallics. Scr Mater 2016;124:108–11.
[28] Edalati K, Matsuda J, Yanagida A, Akiba E, Horita Z. Activation of TiFe for hydrogen storage by plastic deformation using groove rolling and high-pressure torsion: similarities and differences. Int J Hydrogen Energy 2014;39:15589–94.
[29] Ali W, Hao Z, Li Z, Chen G, Wu Z, Lu X, et al. Effects of Cu and Y substitution on hydrogen storage performance of TiFe0.86Mn0.1Y0.1−xCux. Int J Hydrogen Energy 2017;42:16620–31.
[30] Leng H, Yu Z, Yin J, Li Q, Wu Z, Chou K-C. Effects of Ce on the hydrogen storage properties of TiFe 0.9 Mn 0.1 alloy. Int J Hydrogen Energy 2017;42:23731–6.
[31] Kulshreshtha SK, Jayakumar OD, Bhatt KB. Hydriding characteristics of palladium and platinum alloyed FeTi. J Mater Sci 1993;28:4229–33.
[32] Lee SM, Perng TP. Correlation of substitutional solid solution with hydrogenation properties of TiFe1-xMx (M = Ni, Co, Al) alloys. J Alloy Comp 1999;291:254–61.
[33] Chung HS, Lee JY. Effect of partial substitution of Mn and Ni for Fe in FeTi on hydriding kinetics. Int J Hydrogen Energy 1986;11:335–9.
[34] Lee SM, Perng TP. Effect of the second phase on the initiation of hydrogenation of TiFe1−xMx (M = Cr,Mn) alloys. Int J Hydrogen Energy 1994;19:259–63.
[35] Jain P, Gosselin C, Huot J. Effect of Zr, Ni and Zr7Ni10 alloy on hydrogen storage characteristics of TiFe alloy. Int J Hydrogen Energy 2015;40:16921–7.
[36] Lv P, Huot J. Hydrogen storage properties of Ti0.95FeZr0.05, TiFe0.95Zr0.05 and TiFeZr0.05 alloys. Int J Hydrogen Energy 2016;41:22128–33.
[37] Patel AK, Sharma P, Huot J. Effect of annealing on microstructure and hydrogenation properties of TiFe + X wt % Zr (X = 4, 8). Int J Hydrogen Energy 2018;43:6238–43.
[38] Lv P, Huot J. Hydrogenation improvement of TiFe by adding ZrMn2. Energy 2017;138:375–82.
[39] Cheary RW, Coelho AA, Cline JP. Fundamental parameters line profile fitting in laboratory diffractometers. J Res Natl Inst Stand Technol 2004;109:1–25.
[40] Murray JL. The Fe–Ti (Iron-Titanium) system. B Alloy Phase Diagrams 1981;2:320–34.
[41] Fedorov TF, Kuz'ma YB. The titanium-iron-boron system. Izv Akad Nauk SSSR - Neorganicheskiye Mater 1967;3(8):1498–9 (in Russian). TR: Inorg Mater. 1967;8:1307-08.
[42] Shang H, Zhang Y, Li Y, Qi Y, Guo S, Zhao D. Effects of adding over-stoichiometrical Ti and substituting Fe with Mn partly on structure and hydrogen storage performances of TiFe alloy. Renew Energy 2019;135:1481–98.
[43] Guéguen A, Latroche M. Influence of the addition of vanadium on the hydrogenation properties of the compounds TiFe0.9Vx and TiFe0.8Mn0.1Vx (x=0, 0.05 and 0.1). J Alloy Comp 2011;509:5562–6.
[44] Lang J, Eagles M, Conradi MS, Huot J. Hydrogenation rate limiting step, diffusion and thermal conductivity in cold rolled magnesium hydride. J Alloy Comp 2014;583:116–20.
[45] Mintz MH, Zeiri Y. Hydriding kinetics of powders. J Alloy Comp 1994;216:159.
[46] Avrami M. Kinetics of phase change. I: general theory. J Chem Phys 1939;7:1103–12.
[47] Pang Y, Li Q. A review on kinetic models and corresponding analysis methods for hydrogen storage materials. Int J Hydrogen Energy 2016;41:18072–87.